THE JOURNAL OF PHYSICAL CHEMISTRY C

Article

Cite This: J. Phys. Chem. C 2020, 124, 436−445

pubs.acs.org/JPCC

Atomistic Simulation of Ice Nucleation on Silver Iodide (0001) Surfaces with Defects

Golnaz Roudsari, Bernhard Reischl, Olli H. Pakarinen,* and Hanna Vehkamäki

Institute for Atmospheric and Earth System Research/Physics, University of Helsinki, PO Box 64, Helsinki FI-00014, Finland

Supporting Information

ABSTRACT: Small particles of silver iodide (AgI) are known to have excellent ice nucleating capabilities and have been used in rain seeding applications. It is widely believed that the silver-terminated (0001) surface of β-AgI acts as a template for the basal plane of hexagonal ice. However, the (0001) surface of ionic crystals with the wurtzite structure is polar and will therefore exhibit reconstructions and defects. Here, we use atomistic molecular dynamics simulations to study how the presence of defects on AgI(0001) affects the rates and mechanism of heterogeneous ice nucleation at moderate supercooling at −10 °C. We consider AgI(0001) surfaces exhibiting vacancies, step edges, terraces, and pits and compare them to simulations of the corresponding ideal surface. We find that, while point defects have no significant effect on ice nucleation rates, step edges, terraces, and pits reduce both the nucleation and growth rates by up to an order of magnitude. The reduction of the ice nucleation rate correlates well with the fraction of the surface area around the defects where perturbations of the hydration layer hinder the formation of a critical ice nucleus.

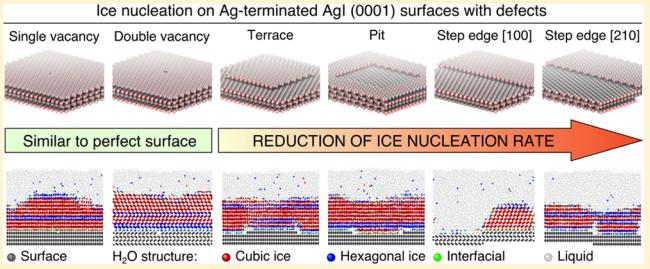

INTRODUCTION

The presence of a seed particle can drastically reduce the supercooling needed for freezing water compared to homogeneous nucleation. This heterogeneous ice nucleation is ubiquitous in nature and plays an important role in cloud formation. For example, mineral dust and organic materials can serve as ice nucleation particles (INPs). The mechanism of heterogeneous ice nucleation depends on a balance between surface morphology and hydrophobicity.[1] On most mineral dust particles, there are only a few active sites for ice nucleation, typically around defects or pits.[2−4]

Silver iodide (AgI) particles are very effective INPs used for rain seeding,[5] and they have been studied both experimentally (see the review by Marcolli et al.[6]) and computationally, focusing on ice nucleation on flat AgI surfaces,[7,8] AgI disks and plates,[9] the effect of surface charge distribution,[10] the effect of defect surface fraction,[11] and water adsorption in slit-like AgI pores.[12] In ambient conditions, both AgI crystals with the wurtzite structure (β-AgI) and zinc blende structure (γ-AgI) are stable. Previous simulations have found that ice could nucleate at the silver-terminated (001) and (111) surfaces of γ-AgI and the silver-terminated (0001) surface of β-AgI.[8] The ice nucleating ability of AgI has been attributed to the (0001) surface of β-AgI acting as a very good template for the basal plane of hexagonal ice (ice I_h) or the equivalent (111) plane of cubic ice (ice I_c)[9] with a lattice mismatch of approximately 2% as illustrated in Figure 1. However, AgI(0001) is a type 3 polar surface[13] and therefore intrinsically unstable. While a recent study showed that the interface with an aqueous solution can stabilize the (0001) surface,[14] reconstructions and defects are still expected to be abundant, as can be seen from electron microscope images of micrometer-sized AgI plate crystals exposing (0001) facets.[15] It is therefore important to investigate how the presence of such defects on AgI(0001) surfaces affects ice nucleation and growth rates. For many other systems, ice nucleates on time scales that are hard to reach in an unbiased atomistic molecular dynamics simulation, making it necessary to utilize a coarse-grained approach using the monatomic (mW) model of water and/or more elaborate simulation techniques, such as seeded nucleation simulations,[16] or advanced sampling techniques such as forward-flux sampling[17] or transition path sampling.[18] In contrast, ice nucleation on AgI typically starts on a timescale of nano-

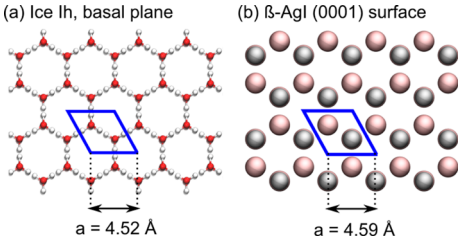

Figure 1. (a) Basal plane of ice I_h and (b) the (0001) surface of β-AgI seen along the c axis of the crystals. The lattice mismatch is less than 2%. O, H, Ag, and I are colored in red, white, silver, and pink, respectively. The hexagonal unit cells are indicated by blue lines.

Received: September 6, 2019
Revised: November 19, 2019
Published: December 11, 2019

DOI: 10.1021/acs.jpcc.9b08502
J. Phys. Chem. C 2020, 124, 436−445

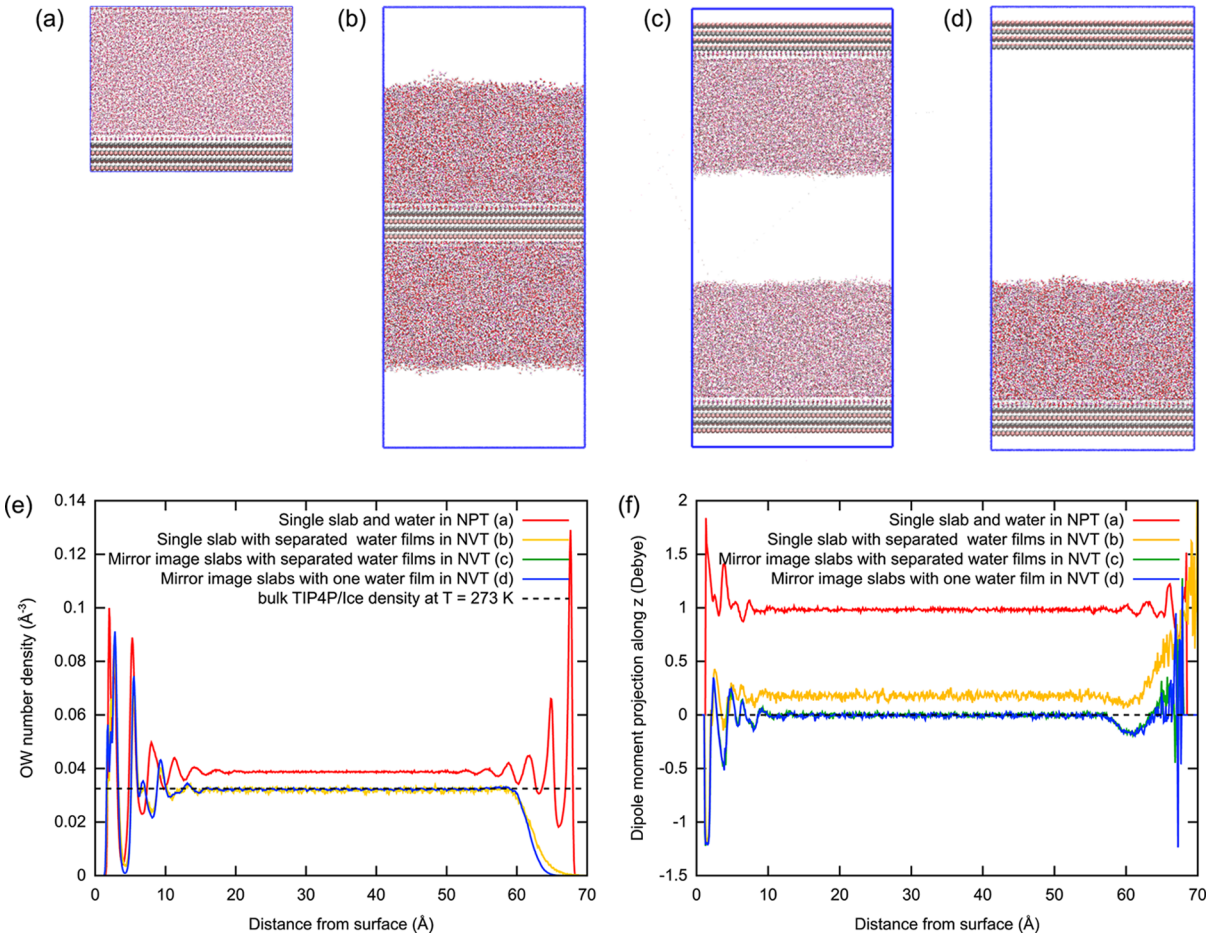

Figure 2. Different simulation setups for an AgI(0001)−water interface (top): (a) slab in contact with bulk water in 3D PBC, (b) slab in contact with two films of water with open surfaces, (c) mirror image geometry with two films of water, and (d) mirror image geometry with only one film of water. (e) Water density profile along z and (f) profile of the projection of the water dipole moment along z observed for the different simulation setups (bottom).

seconds,[8,9] easily accessible in an unbiased molecular dynamics simulation, even for large system sizes.

In this work, we use molecular dynamics (MD) simulations to study the effect of defects, such as vacancies, step edges, terraces, and pits, on ice nucleation on AgI(0001) surfaces.

METHODS

Force Field and Molecular Dynamics Details. Several force fields have been fitted to reproduce bulk crystal structures and the phase diagram of silver iodide (AgI).[19,20] However, the perfect (0001)-terminated AgI slab has an intrinsic dipole moment, and none of these force fields yields a stable surface. In previous ice nucleation simulations, atoms in the AgI surface have therefore either been fixed to bulk positions or constrained by a spring potential. In the present work, all AgI surfaces considered are bulk-terminated and atoms are completely fixed at the positions of an ideal wurtzite crystal with lattice constants of a = 4.58 Å and c = 7.50 Å. The silver and iodide ions only interact with the water molecules, described by the TIP4P/ice model. It reproduces the properties of bulk liquid water very well and yields the correct melting point and coexistence curve between water and ice I at low pressures.[21] The interactions between Ag^+ and I^- ions and TIP4P/ice water molecules are described by the potential of Hale and Kiefer.[22] The ions carry a point charge and a Lennard-Jones interaction with the oxygen atom of water, OW. The Lennard-Jones parameters are ϵ_{Ag-OW} = 2.289 kJ/mol and σ_{Ag-OW} = 3.17 Å and ϵ_{I-OW} = 2.602 kJ/mol and σ_{I-OW} = 3.34 Å for the Ag−OW and I−OW interactions, respectively. Zielke et al. have previously shown that changing the value of the partial charges between ±0.2e and ±0.6e does not have any considerable effect on ice nucleation results on γ-AgI;[8] hence, we also use the original value of ±0.6e from Hale and Kiefer[22] in the present simulations. We do not consider any polarization effects in our electrostatic interactions since the TIP4P/ice water model also has a rigid point charge geometry.[8] The AgI−water interactions were originally fitted in conjunction with a water model based on the ST-2 potential by Stillinger and Rahman.[23] Since we are using a different water potential, we chose to reduce the cutoff distance in the AgI−water interactions to match the cutoff used in the TIP4P/ice potential. All molecular dynamics (MD) simulations were performed using GROMACS software version 5.[24,25] The equations of motion were integrated using the leapfrog algorithm with a time step of 2 fs. Lennard-Jones and real-space electrostatic interactions were cut off at 8.5 Å. The particle mesh Ewald (PME) method[26] was used to calculate long-range electrostatic interactions. The SETTLE algorithm[27] was used to constrain the O−H bond length and H−O−H angle of the water molecules. In *NVT* production runs, the temperature was controlled with a Nosé−Hoover thermostat[28]

DOI: 10.1021/acs.jpcc.9b08502
J. Phys. Chem. C 2020, 124, 436−445

with a relaxation time of 0.4 ps. For *NPT* equilibration runs, a Berendsen thermostat and barostat with time constants of 0.4 and 5 ps, respectively, were used.

Simulation Setup and Treatment of Surface Dipoles. As previously mentioned, the (0001) surface of AgI has an intrinsic dipole moment, which makes this surface challenging to simulate. We have therefore carried out preliminary checks on how different simulation setups, illustrated in Figure 2a–d, affect the behavior of water at the interface to avoid artifacts in the ice nucleation studies. For simplicity, we only considered the perfect (0001) surface of β-AgI at a temperature of $T = 273$ K. The most common setup for simulating a solid–liquid interface is to have a solid slab in contact with a volume of water in a simulation box with 3D periodic boundaries (see Figure 2a). Throughout this work, the ice surface is always considered to lie in the *xy* plane, and *z* is the direction perpendicular to the surface. In order to equilibrate the system, that is, form hydration layers at the interface and reach bulk water density in the central region of the liquid between the two interfaces, one can carry out an *NPT* simulation where the box vectors along *x* and *y* are fixed to the values determined by the crystal's lattice constant, but the box vector along *z* can fluctuate. Allowing for a change of water density is essential during nucleation simulations as well since the densities of water and ice in the TIP4P/ice water model are 0.985 and 0.906 g/mL, respectively.[29] In the case of AgI(0001), this traditional setup does not work as the dipole field leads to attractive forces between periodic images of the slab, "squeezing" the water and significantly increasing its density above the equilibrium value (see Figure 2e). To avoid this artifact, the crystal slab can instead be in contact with sufficiently thick films of water on either side (see Figure 2b). An appropriately chosen vacuum gap between the two films' interfaces on opposite sides, together with a simulation in *NVT* conditions, can ensure that the density of the liquid reaches the proper value in the "bulk" region between the interfaces with the solid or the vacuum (see Figure 2e). However, the dipole field still causes a spurious alignment of water molecules far away from the surface (see Figure 2f). A "mirror image" geometry can be used to effectively cancel the dipole field: two copies of the AgI(0001) slab, mirrored along the *xy* plane, are placed on opposite ends of the simulation box, each in contact with a water film with an open surface and separated by a vacuum gap (see Figure 2c). This setup ensures the correct bulk water density and removes the spurious water orientation (see Figure 2e,f). Finally, to reduce the number of atoms in the simulation, we have also considered a mirror image setup of the crystal slabs but with the water on the upper slab removed (see Figure 2d). This setup gives results identical to the previous setup (see Figure 2e,f) and was therefore chosen for all the nucleation simulations performed in this work.

Silver Iodide Surfaces with Defects. To study the effect of defects on ice nucleation at the silver iodide surface, we consider charge-neutral AgI(0001) surfaces with single or double vacancies, a step edge along [210] and [100], terraces, and pits and compare them to simulations of the corresponding ideal surface. The six different nonideal geometries are illustrated in Figure 3. In the double-vacancy system, an ion pair was removed from the top of the surface, whereas in the single-vacancy system, an Ag^+ ion was removed from the top surface and an I^- ion was removed from the bottom to keep the system charge neutral. In all systems, [100] and [210] crystallographic directions correspond to *x* and *y* directions of the simulation cell, respectively. The mirror image geometry with water only present on top of the lower AgI slab was used (see Figure 2d). The open water surface allows for a change of water density during ice nucleation, even though the simulation box volume is constant. To minimize finite size effects, such as the interaction of the ice nucleus with itself through the periodic boundaries along *x* and *y*, the lateral dimensions of the simulation box are chosen to be quite large (100.76×103.13 Å^2). Also, the film of water on the lower AgI slabs has a thickness of ~60 Å to have a considerable number of bulk-like water molecules and to be able to observe the growth of many layers of ice after the onset of nucleation. The total height of the simulation boxes was 220 Å.

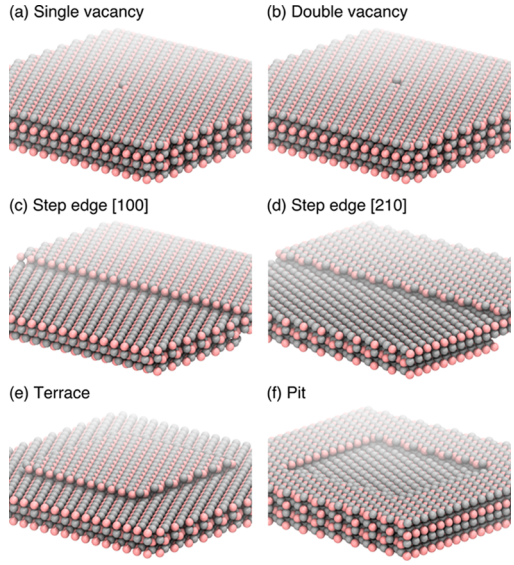

Figure 3. (a–f) Atomistic models of six different AgI(0001) surfaces with defects. Ag^+ and I^- ions are colored in silver and pink, respectively.

RESULTS AND DISCUSSION

To study ice nucleation and growth rates on the perfect surface and surfaces with defects, we analyze snapshots of the MD trajectories taken at every nanosecond using the CHILL+ algorithm[30] to classify each H_2O molecule as cubic ice, hexagonal ice, interfacial ice, or liquid based on its hydrogen bond arrangement. The final frames of each trajectory are shown in Figure S1 in the Supporting Information. By identifying the appearance of critical nuclei and determining the volume of ice formed during the simulations, we are able to determine the ice nucleation and growth rates for each system.

Nucleation Rates. To quantify the effectiveness of the different systems for ice nucleation, we calculate nucleation rates at $T = 263$ K following the procedure presented by Cox et al.[31] By monitoring the size of the largest ice cluster in the system using the CHILL+ algorithm, the induction time is found, which is defined as the time when the ice cluster starts growing monotonously. For each system, 10 individual *NVT* simulations are started with different initial configurations and velocities of the water molecules. The induction times observed are used to calculate the probability $P_{liq}(t)$ of an ensemble of systems to be still in the liquid state after time *t*. As the temperature is 10 °C below the melting point, we expect the probability to decay exponentially. We fit the data using the following equation

DOI: 10.1021/acs.jpcc.9b08502
J. Phys. Chem. C 2020, 124, 436–445

$$P_{liq}(t) = \exp[-(Rt)^{\gamma}] \quad (1)$$

where R shows the decay rate, equal to the nucleation rate, and the exponent γ is a second fitting parameter, as illustrated in Figure 4.

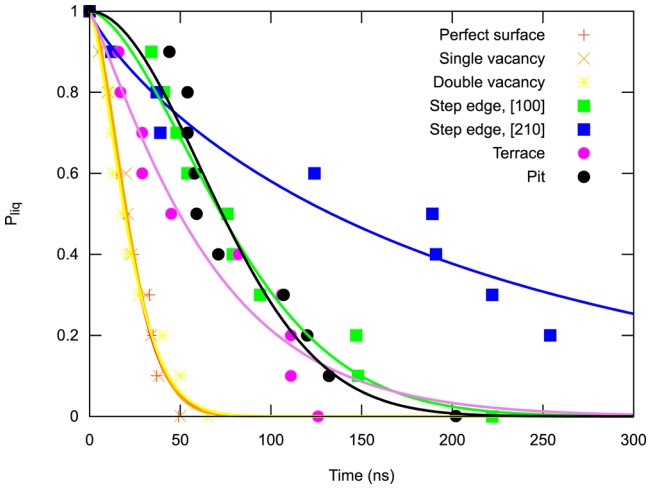

Figure 4. Obtaining ice nucleation rates on different AgI(0001) surfaces from fitting the induction times for ice nucleation in 10 independent molecular dynamics simulations at T = 263 K.

The nucleation rates obtained for the different surfaces are shown in Table 1. The standard errors were obtained from the least-squares error of the fit using eq 1. The surface with a double vacancy and perfect surface exhibit the highest nucleation rates with values of 3.89 × 10^{23} and 3.86 × 10^{23} m^{-2} s^{-1}, respectively. Surfaces with a single Ag vacancy show almost the same nucleation rate (3.75 × 10^{23} m^{-2} s^{-1}). The nucleation rates on surfaces with point defects are very similar to the rate on the perfect surface. The two step edges considered affect the nucleation rate with different severities, leading to rates of 1.06 × 10^{23} and 0.47 × 10^{23} m^{-2} s^{-1} for the step edge along [100] and [210] directions, respectively. Finally, nucleation rates of 1.41 × 10^{23} and 1.09 × 10^{23} m^{-2} s^{-1} were observed for the surface with a terrace or a pit, respectively.

Table 1. Ice Nucleation Rates and Uncertainties on Different AgI(0001) Surfaces with Defects at T = 263 K

system	nucleation rate (×10^{23} m^{-2} s^{-1})
perfect surface	3.86 ± 0.13
single vacancy	3.75 ± 0.12
double vacancy	3.89 ± 0.23
step edge [100]	1.06 ± 0.04
step edge [210]	0.47 ± 0.05
terrace	1.41 ± 0.12
pit	1.09 ± 0.06

These results are quite surprising as, for many surfaces, ice nucleation rates are enhanced by the presence of defects. Here, however, the perfect surface is an excellent template for ice growth due to the very small lattice mismatch between AgI(0001) and the basal plane, and all extended defects considered in this work reduce the nucleation rate. We also note that the nucleation rate on the perfect AgI(0001) surface reported here is roughly eight times smaller compared to a previous study by Glatz and Sarupria.[10] However, the surface area in their simulation was less than 900 Å^2, compared to over 10,000 Å^2 in the present study, which could indicate that their result was influenced by finite size effects. Finally, we also carried out simulations with similar systems at stronger undercooling at T = 258 and 261 K. At these temperatures, the induction times are even shorter and it becomes increasingly difficult to assess the influence of the defect on the nucleation rates.

Nucleation Mechanisms. To better understand the ice nucleation mechanism at the silver iodide surface and, in particular, how the presence of defects affects the possibility to form a critical nucleus at the interface, we compare the hydration layer structure and dynamics on the perfect surface and around the step edge along the [210] direction.

On the perfect surface, the structure of the first hydration layer is very similar to the basal layer of ice (I_h), as shown in Figure 5. Water oxygen atoms are situated at the corners of hexagons coordinating the protruding Ag^+ ion in the surface, that is, directly on top of the subsurface I^- ion. At 273 K, a well-defined second hydration layer is also visible before the changes in water density level off to the constant bulk water density.

To study the dynamics, residence times of water molecules in the first hydration layer were also calculated from MD trajectories using the method suggested by De La Pierre et al.[32] We computed the molecules' survival function

$$P(t) = \int_t^{\infty} E(t')\mathrm{d}t' \quad (2)$$

where $E(t)\mathrm{d}t$ represents the probability for a water molecule to remain coordinated to a surface Ag ion site for a time between t and t + dt. This was then fitted with the sum of two exponentially decaying functions

$$P(t) = a_1\exp(t/\tau_1) + a_2\exp(t/\tau_2) \quad (3)$$

The small time constant τ_1 corresponds to fluctuations in and out of the cutoff distance used to identify water molecules in the first hydration layer, and τ_2 is the actual residence time of the water molecule before an exchange takes place.

While the equilibrium structure of the first hydration layer on the perfect surface is similar to the basal plane of ice I_h and closely resembles the first layer of ice on the perfect surface at 263 K (see Figure 5a), at 273 K, the structure is still surprisingly dynamic with water exchanging on a time scale of ∼2.0 ns at T = 273 K, as calculated from the survival probabilities in eq 2.

As can be seen in Figure 6, the pattern of the first hydration layer is perturbed by the presence of the step edge, and the average time scale of water exchange is reduced to ∼1.8 ns on the surface containing the step edge. In order to quantify the spatial extent of the hydration layer perturbation around the step edge and link it to the observed nucleation rate, we have calculated the average deviation d of first-hydration layer, water-molecule oxygen from its ideal position as a function of the position along x, the direction perpendicular to the step edge (see Figure 6b)

$$d = \sqrt{(x_O - x_I)^2 + (y_O - y_I)^2} \quad (4)$$

where x_O and y_O are the x and y positions of the oxygen atoms and x_I and y_I are the subsurface iodide ions' x and y positions. While on the perfect surface, the average disturbance of water

DOI: 10.1021/acs.jpcc.9b08502
J. Phys. Chem. C 2020, 124, 436−445

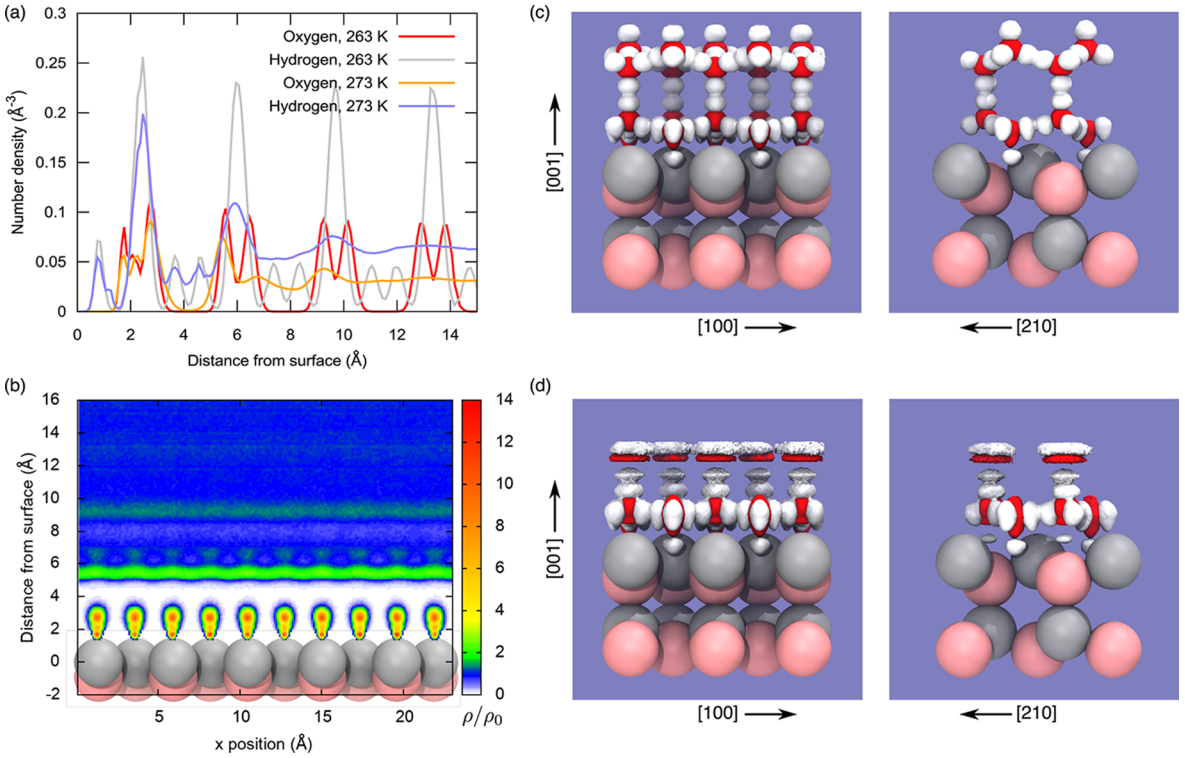

Figure 5. AgI(0001) hydration structure. (a) Number density of oxygen and hydrogen atoms as a function of the distance from the perfect AgI(0001) surface at 273 and 263 K. (b) Water oxygen atom density map projection in the *xz* plane over the AgI(0001) surface. The number density is expressed in units of the equilibrium water density at T = 273 K, $\rho_0 \approx 0.032$ Å^{-3}, shown in blue. Surface Ag^+ and I^- ions are colored in silver and pink, respectively. First and second hydration layer oxygen (red) and hydrogen (white) density isosurface plots over the perfect surface at (c) 263 and (d) 273 K. The isosurfaces shown correspond to $\rho = 25\,\rho_0$.

patterning is only ~0.3 Å, this value rises to a maximum of ~0.7 Å over the step edge located at x = 50 Å. The spatial extent of the perturbation along x is ±5.3 Å on either side of the step edge. Values were averaged from three independent 10 ns long trajectories.

Combining the information about the spatial extent of hydration layer perturbation due to the presence of a defect with the average radius of the initial ice clusters at nucleation sites on the surfaces ($r_c \approx 10.3$ Å) allows us to build a very simple model to predict the reduction in nucleation rates compared to the perfect surface, based solely on the surface area excluded for the formation of a critical nucleus around a defect with a certain geometry. As can be seen in Figure 7, these predicted nucleation rates agree surprisingly well with the nucleation rates obtained from molecular dynamics simulations. The result agrees qualitatively with a recent study where ice nucleation on AgI(0001) was also shown to be suppressed by a large surface fraction of defects.[11]

Topological Analysis of the Interfacial Hydrogen-Bond Network. In the recent study by Prerna et al., the surface fraction of defects on AgI(0001) has been shown to affect the hydrogen bond network topology and the ratio of double-diamond cages (DDCs) and hexagonal cages (HCs).[11] While this topological classification is very similar to the analysis using the CHILL+ algorithm in bulk ice, it is advantageous for the analysis of interfacial ice as it can directly classify molecules that are not in a tetrahedral arrangement as that belonging to DDC or HC cages. We have implemented the topological ring analysis by King[33] and identified HCs and DDCs as previously described by Haji-Akbari and Debenedetti[34] to study the hydrogen bond network topology in the two double layers adjacent to the AgI surfaces in the last frame of each trajectory. The results of the analysis are summarized in Figure S2 in the Supporting Information. We find that, for the perfect surface and the surfaces with point defects, only either HCs or DDCs are present with the former being more frequent (7/10 for perfect and single vacancy surfaces and 6/10 for the surface with a double vacancy). For surfaces with terraces, ice nucleation starts on the flat surface around the terrace 8 times out of 10. Here, 7/10 systems contain both HCs and DDCs, 3/10 systems contain only HCs, and ice nucleates 4 times as HCs and 6 times as DDCs. For surfaces with pits, ice nucleation always starts outside the defect. Each system shows both HCs and DDCs, and in nine cases, only HCs are present outside the defect and in one case only DDC, and the topology inside the pit is always opposite of the one on the flat surface outside. On the step edges along [100], ice always nucleates on the upper terrace with HC and DDC occurring equally often. In one system, only DDCs are present; in two systems, HCs and DDCs; in three systems, HCs and liquid water; and in four systems, DDCs and water. On the step edges along [210], we observed seven nucleation events on the upper terrace and one on the lower. In two cases, the volumes of ice formed are still too small to determine a critical nucleus properly. However, all eight nucleation events occurred as HCs. A number of 5/10 systems contain only HCs; one system contains both HCs and DDCs and three systems, HCs and liquid water.

The topological analysis confirms that the presence of extended defects promotes the presence of both DDCs and HCs close to the surface, contrary to the perfect surface or the two surfaces with point defects where stacking faults between

DOI: 10.1021/acs.jpcc.9b08502
J. Phys. Chem. C 2020, 124, 436−445

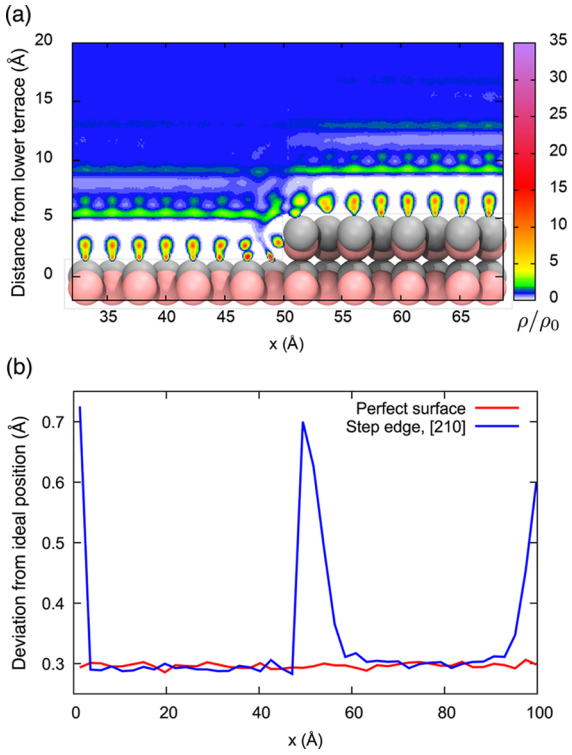

Figure 6. (a) Water oxygen atom density map projection in the *xz* plane over the AgI(0001) surface with a step edge along [210]. The number density is expressed in units of the equilibrium water density at T = 263 K, $\rho_0 \approx 0.032$ Å^{-3}, shown in blue. Surface Ag^+ and I^- ions are colored in silver and pink, respectively. (b) Disturbance of the water patterning in the first hydration layer with respect to the surface lattice over a perfect surface (red line) and a surface with a step edge along [210] (blue line).

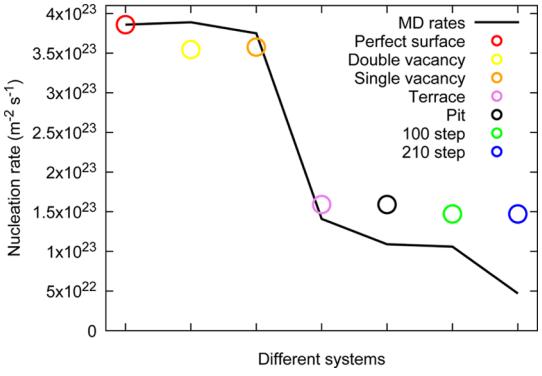

Figure 7. Ice nucleation rates obtained by scaling the nucleation rate on the perfect surface by the fraction of the surface area exhibiting perfect water patterning (colored circles), compared to nucleation rates obtained from molecular dynamics simulations on the respective nonideal surface (black line).

cubic and hexagonal ice only appear at a later stage. The analysis also indicates that, when comparing the step edges along [100] and [210] or the pit and terrace, which have the same spatial extents, the respective occurrences of HCs and DDCs are different. However, due to the number of different structures observed for each of these systems and the relatively limited sample size, we cannot directly correlate the reduction in nucleation rates with, for example, the ratio of DDCs and HCs, as proposed by Prerna et al.[11]

Ice Growth Rates. We determined ice growth rates for the perfect surface and the surfaces with defects in terms of the volume of ice or the thickness of the ice layer grown per unit of time.

Growth by Volume. To calculate the volume of ice, we determine the number of H_2O molecules classified as hexagonal or cubic ice, N_{C+H}, in each frame of the trajectory using the CHILL+ algorithm and multiplying by the molecular volume of ice

$$V_{ice} = \frac{N_{C+H} N_A M}{\rho_{ice}} \tag{5}$$

where N_A is Avogadro's constant, M is the molar mass of the water molecule, and ρ_{ice} is the density of ice. Examples of growth curves by volume can be found in Figure 9 in the section on ice growth mechanisms.

For each system, we determine the average growth rate from linear fits to the ice volume signal after the induction time for the 10 individual simulations and normalize by the surface area. We can mostly observe a steady increase in the size of the nucleated ice clusters and eventual transition into layer-by-layer growth once the clusters interact with themselves through periodic boundaries along x and y. For each system, the 10 individual simulations with different initial configurations show roughly similar growth rates, but differences exist due to the stochastic appearance of stacking faults that, in some cases, can hinder the layer-by-layer growth.

Average ice growth rates by volume and their standard errors for all systems at T = 263 K are shown in Table 2. For

Table 2. Average Ice Growth Rates on Different AgI(0001) Surfaces with Defects at T = 263 K[a]

system	growth rate by volume (Å ns^{-1})	growth rate by layers (Å ns^{-1})
perfect surface	0.300 ± 0.023	0.859 ± 0.062
single vacancy	0.306 ± 0.017	0.877 ± 0.048
double vacancy	0.305 ± 0.031	0.823 ± 0.068
step edge [100]	0.032 ± 0.002	0.343 ± 0.047
step edge [210]	0.033 ± 0.012	0.275 ± 0.054
terrace	0.138 ± 0.032	0.387 ± 0.048
pit	0.267 ± 0.016	0.589 ± 0.082

[a]Growth rates are calculated from the change of ice volume or number of ice layers as a function of time (1 Å ns^{-1} = 0.1 m s^{-1}).

unobstructed, layer-by-layer growth, such as on the perfect surface or the surface with a single or double vacancy, we can determine the highest growth rate of approximately 0.3 Å ns^{-1}. This value is in good agreement with previous work[7] carried-out AgI(0001) surfaces at a similar 10 K supercooling and lower than the growth rate of 0.7 Å ns^{-1} obtained in a simulation of ice on ice growth.[35] The slower growth on AgI has been attributed to the small lattice mismatch between the basal plane of ice I_h and the (0001) surface of AgI.[7,35] Experiments on a thin layer of ice show a growth rate of approximately 0.3 Å ns^{-1} at 263 K,[36,37] similar to the growth rate on the perfect AgI surface reported in this work. The systems with step edges along [100] and [210] directions both show similar growth rates of approximately 0.03 Å ns^{-1}, although the [210] step shows much more variability between individual simulations, as can be seen from the reported standard errors. In addition, for the system with a step edge along [210], induction times were very long, and in two

DOI: 10.1021/acs.jpcc.9b08502
J. Phys. Chem. C 2020, 124, 436−445

simulations, only a small volume of ice had formed after 300 ns. Growth rates of 0.138 and 0.267 Å ns^{-1} are observed for the surface with a terrace or a pit, respectively.

Growth by Ice Layer Thickness. Since ice eventually grows layer-by-layer on a flat surface in periodic boundary conditions, the growth rate can also be determined by counting the number of layers of ice formed per time. To determine the number of ice layers in a given frame of the trajectory, we calculate the number density profiles along the z axis perpendicular to the surface for cubic and hexagonal ice as well as interfacial and liquid water. Figure 8 shows an example

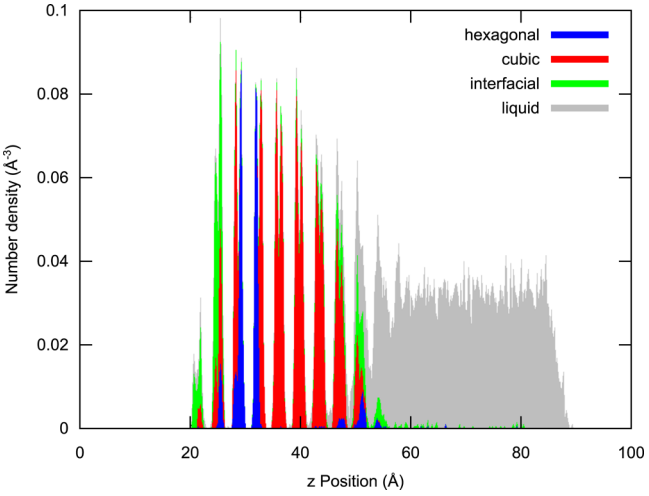

Figure 8. Number density of H_2O molecules along the z axis perpendicular to the surface with the fractions of cubic and hexagonal ice and interfacial and liquid water, colored in red, blue, green, and gray, respectively.

of the number density of water molecules along the z direction during ice growth on a perfect AgI(0001) surface. Each time the sum of the densities of hexagonal and cubic ice in a number density double peak crosses the value of 0.01, a new layer of ice is counted. The total ice thickness is determined by multiplying the number of layers with the thickness of an ice bilayer. The growth rates by ice layer thickness and their standard errors are reported in Table 2. It should be noted that our choice of a small number density cutoff leads to a different definition of the growth rate compared to the volume growth rate, that is, the signal follows more accurately the actual height of ice layers, even for hemispherical clusters, and leads to clearly higher growth rate values than the volume growth rates whenever ice does not grow layer-by-layer. Nevertheless, the relative growth rates between different systems agree reasonably well with the growth rates determined by using the volume of ice as the growth signal. For the perfect, single vacancy, and double vacancy systems, the growth rates are higher than for step edge, terrace, and pit systems.

Growth Mechanisms. During growth of ice, stacking faults between domains of ice I_h and I_c will appear in a stochastic fashion. However, since we have simulated 10 individual trajectories for ice nucleation and growth on each system, we have gathered some statistics that allow us to relate the presence of a certain defect type to changes in the growth mechanism. In Figure 9, we relate changes in the growth rates to the atomistic details of the ice structure determined from the analysis with the CHILL+ algorithm for a perfect surface, surfaces with step edges along [100] and [210], and a surface with a pit. Snapshots of the final configuration of each simulation, analyzed with the CHILL+ algorithm, are also shown in Figure S1 in the Supporting Information.

On the perfect surface, once a complete bilayer of ice has formed, ice growth proceeds mostly layer-by-layer with both ice I_c and I_h appearing in a stacking disordered fashion, similar to growth of pure ice.[38] The growth of a single phase of ice proceeds at an almost constant rate of 0.4 Å ns^{-1}, and we will refer to this as "ideal growth" in the following. Once a stacking fault nucleates, the growth slows down until a clear grain boundary between the two phases across the periodic boundaries of the system has been established, and after which, the growth accelerates again. This mechanism where the system grows alternating between two growth rates is illustrated in Figure 9a. The surface with vacancies essentially shows the same behavior as the perfect surface. On the surface with a double vacancy, we also sometimes observed the nucleation of a stacking fault at the defect site. On the surfaces with step edges, ice nuclei can appear almost simultaneously on both terraces or separately in time, and defining induction times and growth rates is somewhat ambiguous. In every simulation, ice nucleated on the terraces away from the step edge. In principle, the first hydration layer on the upper terrace is at a similar height as the second hydration layer on the lower terrace (see Figure 6a), and a continuous layer of ice connecting through the periodic boundaries could form at this height. However, in case growth starts at similar times but with different types of stacking of ice phases, a stacking fault above the step edge will result, hindering the transition into ideal growth, even after the initially separate volumes of ice have reached the same height (see Figure 9a). If ice nucleates on one terrace only, growth of ice is limited once the step edges are reached, leading to the formation of a half-cylindrical volume of ice connecting through the periodic boundaries, as shown in Figure 9c for a step edge along [100]. In this particular case, nucleation on the lower terrace happens much later, but eventually, a new volume of ice connects to the half-cylinder on the upper terrace through a stacking fault. For the systems with a pit, the nucleation happens typically outside the pit, and several layers of ice can form before ice nucleates inside the pit and eventually connects to the remaining volume, as shown in Figure 9d.

CONCLUSIONS

In this work, we studied the effect of surface defects on the heterogeneous nucleation of ice at the (0001) surface of β-AgI using atomistic molecular dynamics simulations at T = 263 K. The presence of defects reduces both the nucleation rate and growth rate with a clear correlation between the dimensionality of the defects and the severity of the reduction; while single and double vacancies have no significant effect, the presence of step edges, terraces, and pits reduces nucleation and growth rates by up to an order of magnitude. However, it is important to note that even surfaces with these last three defect types still exhibit good ice nucleation abilities at very moderate undercooling.

The simulation results show that the β-AgI(0001) surface enhances the formation of a critical nucleus by enforcing its hexagonal structure on the first hydration layer. On the perfect surface, water molecule oxygen atoms in the first hydration layer are hexagonally arranged around the protruding silver ion in the surface. In the proximity of defects such as a step edge, there are significant deviations from these ideal positions,

DOI: 10.1021/acs.jpcc.9b08502
J. Phys. Chem. C 2020, 124, 436−445

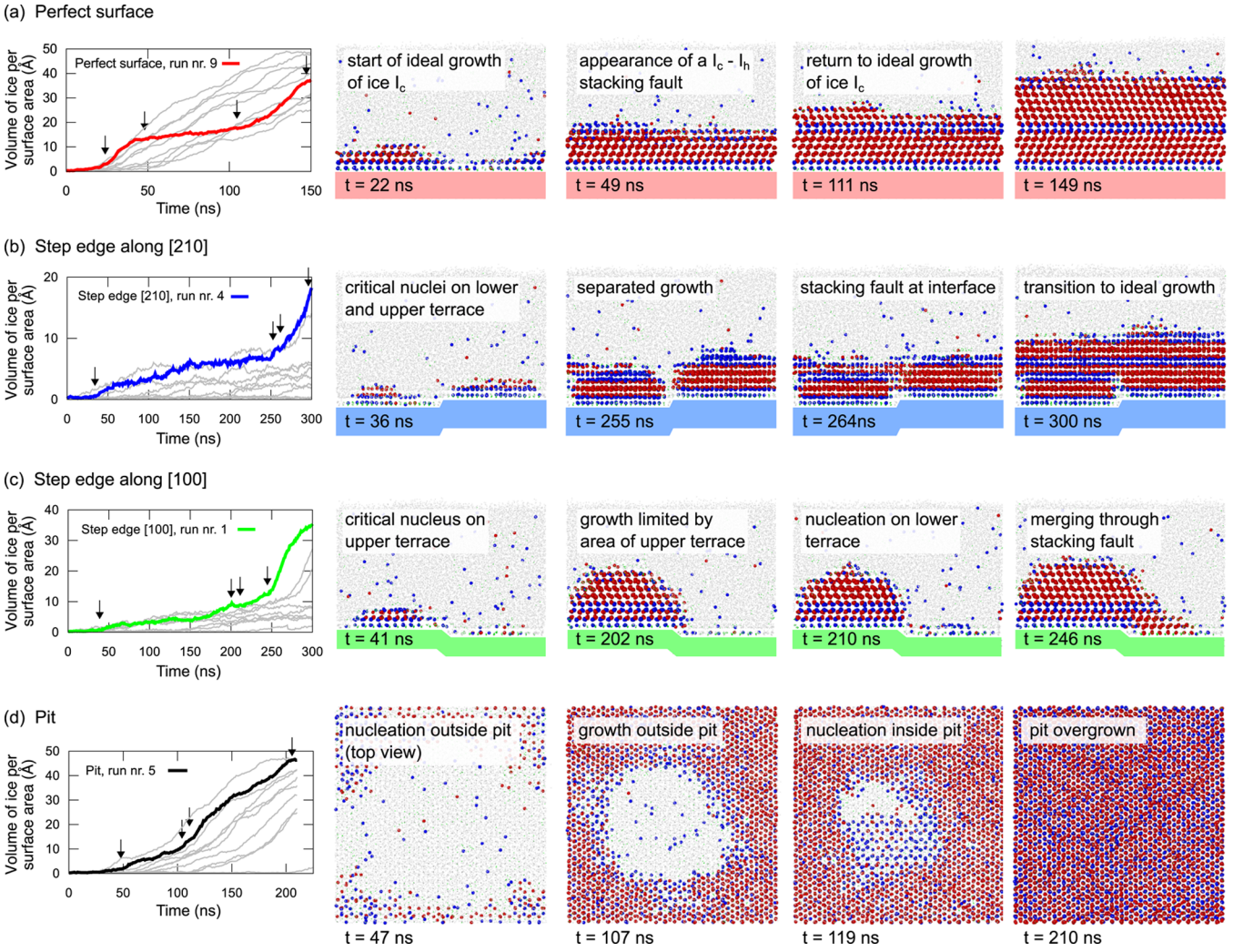

Figure 9. Examples of the atomistic details of ice growth on (a) perfect AgI(0001) surfaces, surfaces with step edges along (b) [210] or (c) [100], and (d) a surface with a pit. The figures on the left-hand side show the ice growth curves for the 10 different simulations for each system (gray lines). One simulation run is highlighted in color, and four snapshots of this particular MD trajectory taken at times indicated by the black arrows are shown next to each figure. In these snapshots, water molecules have been color-coded as cubic ice (red), hexagonal ice (blue), interfacial (green), and liquid (gray) to illustrate the different growth mechanisms. In panels (a)−(c), the system is shown in the side view, whereas the pit system in the bottom panel (d) is shown in the top view.

hindering the formation of critical ice nuclei. A very simple model where the nucleation rate on the perfect surface is scaled by the fraction of the surface area available for nucleation, excluding the area around the defects, gives good agreement with the nucleation rates obtained from molecular dynamics simulations of the different surfaces with defects. However, the model obviously cannot predict differences caused by atomistic details of a defect, such as the different nucleation rates observed in molecular dynamics simulations of surfaces with step edges along [100] or [210] directions. An analysis of the interfacial hydrogen bond network reveals differences in occurrences of hexagonal (HCs) and double-diamond cages (DDCs) for extended defects of similar spatial extent but fails to provide a direct explanation for the reduction in nucleation rates. However, the extended defects clearly promote the combination of HCs and DDCs at the interface, contrary to the perfect surface and surfaces with point defects where only a single type of network is observed.

Our simulations show that the growth of ice essentially proceeds layer-by-layer once the nucleus has covered the entire interface. The rate is highest when ice grows uniformly, either as ice I_h or I_c. The appearance of stacking faults, which reduces the growth rate, is enhanced by the presence of defects in the surface.

Finally, we would like to note that most computational studies of heterogeneous ice nucleation on AgI, including the present work, have considered the (0001) surface because of its ability to nucleate ice on a time scale accessible to atomistic simulation. The fact that this surface is intrinsically unstable because of its dipole requires some brute force approaches (constraining atoms to bulk lattice positions and using a mirror image geometry to cancel the dipole field), which clearly indicates that this type of model is not a good representation of the actual AgI surfaces that are responsible for the material's remarkable ice nucleating abilities. Future studies should address this issue and put an emphasis on developing more realistic models of (0001) surfaces without a dipole, for example, by considering the presence of ions in the water[14] or more complex crystal geometries[39] and surface reconstructions.[40]

DOI: 10.1021/acs.jpcc.9b08502
J. Phys. Chem. C 2020, 124, 436−445

■ ASSOCIATED CONTENT

Supporting Information

The Supporting Information is available free of charge at https://pubs.acs.org/doi/10.1021/acs.jpcc.9b08502.

Ice structures analyzed with the CHILL+ algorithm in the last frame of each of the 10 molecular dynamics trajectories obtained for each of the seven AgI(0001) surfaces with defects and the top view of the hydrogen bond network within the first two double layers of interfacial ice for each surface, showing hexagonal cages (HCs), double-diamond cages (DDCs), and mixed cages in the ice structure (PDF)

■ AUTHOR INFORMATION

Corresponding Author

*E-mail: olli.pakarinen@helsinki.fi.

ORCID

Golnaz Roudsari: 0000-0002-7811-8514
Bernhard Reischl: 0000-0001-7333-4923
Olli H. Pakarinen: 0000-0002-5535-3941
Hanna Vehkamäki: 0000-0002-5018-1255

Notes

The authors declare no competing financial interest.

■ ACKNOWLEDGMENTS

This work was supported by the National Center of Meteorology (NCM), Abu Dhabi, UAE, under the UAE Research Program for Rain Enhancement Science, the Academy of Finland Center of Excellence program (grant no. 307331) and ARKTIKO project no. 285067 ICINA, the University of Helsinki, Faculty of Science, ATMATH project, and ERC grant no. 692891-DAMOCLES. Supercomputing resources were provided by the CSC−IT Center for Science, Ltd., Finland. Any opinions, findings, and conclusions or recommendations expressed in this material are those of the authors and do not necessarily reflect the views of the National Center of Meteorology, Abu Dhabi, UAE, funder of the research.

■ REFERENCES

(1) Fitzner, M.; Sosso, G. C.; Cox, S. J.; Michaelides, A. The Many Faces of Heterogeneous Ice Nucleation: Interplay Between Surface Morphology and Hydrophobicity. *J. Am. Chem. Soc.* **2015**, *137*, 13658−13669.

(2) Kiselev, A.; Bachmann, F.; Pedevilla, P.; Cox, S. J.; Michaelides, A.; Gerthsen, D.; Leisner, T. Active Sites in Heterogeneous Ice Nucleation - the Example of K-rich Feldspars. *Science* **2017**, *355*, 367−371.

(3) Murray, B. J. Cracking the Problem of Ice Nucleation. *Science* **2017**, *355*, 346−347.

(4) Holden, M. A.; Whale, T. F.; Tarn, M. D.; O'Sullivan, D.; Walshaw, R. D.; Murray, B. J.; Meldrum, F. C.; Christenson, H. K. High-speed Imaging of Ice Nucleation in Water Proves the Existence of Active Sites. *Sci. Adv.* **2019**, *5*, No. eaav4316.

(5) Vonnegut, B. The Nucleation of Ice Formation by Silver Iodide. *J. Appl. Phys.* **1947**, *18*, 593−595.

(6) Marcolli, C.; Nagare, B.; Welti, A.; Lohmann, U. Ice Nucleation Efficiency of AgI: Review and New Insights. *Atmos. Chem. Phys.* **2016**, *16*, 8915−8937.

(7) Fraux, G.; Doye, J. P. K. Note: Heterogeneous Ice Nucleation on Silver-iodide-like Surfaces. *J. Chem. Phys.* **2014**, *141*, 216101.

(8) Zielke, S. A.; Bertram, A. K.; Patey, G. N. A Molecular Mechanism of Ice Nucleation on Model AgI Surfaces. *J. Phys. Chem. B* **2014**, *119*, 9049−9055.

(9) Zielke, S. A.; Bertram, A. K.; Patey, G. N. Simulations of Ice Nucleation by Model AgI Disks and Plates. *J. Phys. Chem. B* **2016**, *120*, 2291−2299.

(10) Glatz, B.; Sarupria, S. The Surface Charge Distribution Affects the Ice Nucleating Efficiency of Silver Iodide. *J. Chem. Phys.* **2016**, *145*, 211924.

(11) Prerna; Goswami, R.; Metya, A. K.; Shevkunov, S. V.; Singh, J. K. Study of ice nucleation on silver iodide surface with defects. *Mol. Phys.* **2019**, 3651.

(12) Shevkunov, S. V. Structure of Water Adsorbed in Slit-shaped Pores of Silver Iodide Crystal. *Comput. Theor. Chem.* **2016**, *1084*, 1−16.

(13) Tasker, P. W. The Stability of Ionic Crystal Surfaces. *J. Phys. C: Solid State Phys.* **1979**, *12*, 4977−4984.

(14) Sayer, T.; Cox, S. J. Stabilization of AgI's Polar Surfaces by the Aqueous Environment, and its Implications for Ice Formation. *Phys. Chem. Chem. Phys.* **2019**, *21*, 14546−14555.

(15) Kuang, Q.; Zheng, X.; Yang, S. AgI Microplate Monocrystals with Polar 0001 Facets: Spontaneous Photocarrier Separation and Enhanced Photocatalytic Activity. *Chem. - Eur. J.* **2014**, *20*, 2637−2645.

(16) Pedevilla, P.; Fitzner, M.; Sosso, G. C.; Michaelides, A. Heterogeneous Seeded Molecular Dynamics as a Tool to Probe the Ice Nucleating Ability of Crystalline Surfaces. *J. Chem. Phys.* **2018**, *149*, No. 072327.

(17) Sosso, G. C.; Li, T.; Donadio, D.; Tribello, G. A.; Michaelides, A. Microscopic Mechanism and Kinetics of Ice Formation at Complex Interfaces: Zooming in on Kaolinite. *J. Phys. Chem. Lett.* **2016**, *7*, 2350−2355.

(18) Lupi, L.; Peters, B.; Molinero, V. Pre-ordering of Interfacial Water in the Pathway of Heterogeneous Ice Nucleation Does not Lead to a Two-step Crystallization Mechanism. *J. Chem. Phys.* **2016**, *145*, 211910.

(19) Rains, C. A.; Ray, J. R.; Vashishta, P. Phase Transformations and Polytypism in Silver Iodide: A Molecular-Dynamics Study. *Phys. Rev. B* **1991**, *44*, 9228−9239.

(20) Niu, H.; Jing, Y.; Sun, Y.; Aluru, N. R. Ab Initio Based Interionic Potential for Silver Iodide. *Solid State Ionics* **2018**, *325*, 102−111.

(21) Abascal, J. L. F.; Sanz, E.; García Fernández, R.; Vega, C. A Potential Model for the Study of Ices and Amorphous Water: TIP4P/Ice. *J. Chem. Phys.* **2005**, *122*, 234511.

(22) Hale, B. N.; Kiefer, J. Studies of H2O on beta-AgI Surfaces - An Effective Pair Potential Model. *J. Chem. Phys.* **1980**, *73*, 923−933.

(23) Stillinger, F. H.; Rahman, A. Improved Simulation of Liquid Water by Molecular Dynamics. *J. Chem. Phys.* **1974**, *60*, 1545−1557.

(24) van der Spoel, D.; Lindahl, E.; Hess, B.; Groenhof, G.; Mark, A. E.; Berendsen, H. J. C. GROMACS: Fast, Flexible, and Free. *J. Comput. Chem.* **2005**, *26*, 1701−1718.

(25) Berendsen, H. J. C.; van der Spoel, D.; van Drunen, R. GROMACS: A Message-passing Parallel Molecular Dynamics Implementation. *Comput. Phys. Commun* **1995**, *91*, 43−56.

(26) Essmann, U.; Perera, L.; Berkowitz, M. L.; Darden, T.; Lee, H.; Pedersen, L. G. A Smooth Particle Mesh Ewald Method. *J. Chem. Phys.* **1995**, *103*, 8577−8593.

(27) Miyamoto, S.; Kollman, P. A. Settle - an Analytical Version of the Shake and Rattle Algorithm for Rigid Water Models. *J. Comput. Chem.* **1992**, *13*, 952−962.

(28) Nosé, S. A Molecular Dynamics Method for Simulations in the Canonical Ensemble. *Mol. Phys.* **1984**, *52*, 255−268.

(29) Abascal, J. L. F.; Vega, C. A General Purpose Model for the Condensed Phases of Water: TIP4P/2005. *J. Chem. Phys.* **2005**, *123*, 234505.

(30) Nguyen, A. H.; Molinero, V. Identification of Clathrate Hydrates, Hexagonal Ice, Cubic Ice, and Liquid Water in Simulations: the CHILL+ Algorithm. *J. Phys. Chem. B* **2015**, *119*, 9369−9376.

DOI: 10.1021/acs.jpcc.9b08502
J. Phys. Chem. C 2020, 124, 436−445

(31) Cox, S. J.; Kathmann, S. M.; Slater, B.; Michaelides, A. Molecular Simulations of Heterogeneous Ice Nucleation. I. Controlling Ice Nucleation Through Surface Hydrophilicity. *J. Chem. Phys.* **2015**, *142*, 184704.
(32) De La Pierre, M.; Raiteri, P.; Gale, J. D. Structure and Dynamics of Water at Step Edges on the Calcite $\{10\bar{1}4\}$ Surface. *Cryst. Growth Des.* **2016**, *16*, 5907−5914.
(33) King, S. V. Ring Configurations in a Random Network Model of Vitreous Silica. *Nature* **1967**, *213*, 1112−1113.
(34) Haji-Akbari, A.; Debenedetti, P. G. Direct Calculation of Ice Homogeneous Nucleation Rate for a Molecular Model of Water. *Proc. Natl. Acad. Sci. U. S. A.* **2015**, *112*, 10582−10588.
(35) Rozmanov, D.; Kusalik, P. G. Temperature Dependence of Crystal Growth of Hexagonal Ice (I_h). *Phys. Chem. Chem. Phys.* **2011**, *13*, 15501−15511.
(36) Xu, Y.; Petrik, N. G.; Smith, R. S.; Kay, B. D.; Kimmel, G. A. Growth Rate of Crystalline Ice and the Diffusivity of Supercooled Water from 126 to 262 K. *Proc. Natl. Acad. Sci. U. S. A.* **2016**, *113*, 14921−14925.
(37) Amaya, A. J.; Pathak, H.; Modak, V. P.; Laksmono, H.; Loh, N. D.; Sellberg, J. A.; Sierra, R. G.; McQueen, T. A.; Hayes, M. J.; Williams, G. J.; et al. How Cubic Can Ice Be? *J. Phys. Chem. Lett.* **2017**, *8*, 3216−3222.
(38) Lupi, L.; Hudait, A.; Peters, B.; Grünwald, M.; Mullen, R. G.; Nguyen, A. H.; Molinero, V. Role of Stacking Disorder in Ice Nucleation. *Nature* **2017**, *551*, 218−222.
(39) Li, H.; Geelhaar, L.; Riechert, H.; Draxl, C. Computing Equilibrium Shapes of Wurtzite Crystals: The Example of GaN. *Phys. Rev. Lett.* **2015**, *115*, No. 085503.
(40) Mora-Fonz, D.; Lazauskas, T.; Farrow, M. R.; Catlow, C. R. A.; Woodley, S. M.; Sokol, A. A. Why Are Polar Surfaces of ZnO Stable? *Chem. Mater.* **2017**, *29*, 5306−5320.

DOI: 10.1021/acs.jpcc.9b08502
J. Phys. Chem. C 2020, 124, 436−445